

# Application of the CLEAN Algorithm to Three Dimensional Coded Aperture Imaging

Kevin Byard

*School of Economics, Faculty of Business, Economics and Law, Auckland University of Technology, Auckland 1142, New Zealand*

---

## Abstract

An iterative technique for the removal of artifacts caused by the near field effects of a coded aperture imaging system is presented. The technique, which we call z-Clean, first locates high energy sources within a three dimensional field of view using a least squares method and then removes the artifacts using a method similar to that of the CLEAN algorithm used in radio astronomy, but instead operating in the detector shadowgram domain rather than the final image domain. Computer simulations were performed of observations of four point sources of different intensities and at different depths from the detector. Both a continuous detector of 1cm FWHM detection capability and a pixellated detector with 0.2cm square pixels were investigated using a Modified Uniformly Redundant Array coded aperture of element size 0.6cm. The efficacy of the z-Clean technique for artifact removal is demonstrated for both detector types for the three strongest sources of 100kBq, 50kBq and 10kBq using plane separations of 2cm, 1cm, 0.5cm and 0.1cm, to leave only small ghosts lying up to around 2cm from the reconstructed source depth. For twenty trials of each observation, the three strongest sources are reconstructed no further than 0.7cm from the closest plane with many being from 0cm to 0.5cm for both detector types. The depth location for all three strongest sources using both detector types is no worse than 0.5cm from the actual source depth and is in most cases much better, being closer than 0.1cm for the strongest source at plane separations of 1cm, 0.5cm and 0.1cm. z-Clean was not able to remove the artifacts nor determine accurately the depth of the weakest source of 5kBq and in general sources that experience a phasing error are less accurately located although still better than 0.5cm from the actual source depth for all such cases. The artifact removal and very good depth location come at the expense of an impact on the signal to noise

ratio (SNR) of the sources. For the strongest source and using the continuous detector the SNR increases unexpectedly to give values higher than that for observations made only in the critical plane due to the ghosting of this source in other planes at different depths. For all other cases there is a decrease in SNR which is more marked for finer plane separations and for weaker sources.

*Keywords:* coded aperture, three dimensional imaging, tomography, gamma ray imaging, image processing

---

## 1. Introduction

Coded aperture imaging has become the major technique for forming images in the high energy domain [1, 2, 3, 4]. In this technique, an aperture consisting of opaque and transparent elements is placed between a photon emitting source and a position sensitive detector. The result is a shadowgram on the detector, which in some applications can be saved on computer as a dataset consisting of a set of Cartesian coordinates for each count on the detector - a form known as *list mode* - and in others may instead be stored as a matrix of counts in the form of pixels. We hereafter refer to a detector operating in list mode as *continuous* and a detector consisting of pixels as *pixellated*. The detector shadowgram needs to be subsequently decoded to produce a reconstructed image of the source distribution. The coded aperture technique was originally proposed for high energy astronomical imaging [4] including X-rays [5] and gamma-rays [6] where the incoming radiation effectively comes from infinity and therefore rays from a point source that reach the detector are parallel to each other. This means that the object distribution is essentially a flat two-dimensional (2D) field with the decoded image being a similarly flat reconstruction of the source distribution.

However other applications of coded apertures have also been proposed, many using near field optics including medical imaging [7, 8] and land mine detection [9]. In the near field the object is placed close to the detector, and so the rays from a point in the object diverge giving rise to different problems compared to the far field. The near field itself may be thought of as a stack of 2D *planes*, each parallel to the aperture and detector but lying at different distances from the detector [8]. We hereafter refer to the perpendicular distance of a point or a plane from the detector as its *depth*. In tomography an attempt is made to ascertain the source distribution in each plane from the detector shadowgram and hence produce an overall three-dimensional

29 (3D) image. To this end a number of studies into tomographical imaging  
 30 have been conducted [8, 10, 11, 12, 13]. While it is possible to create images  
 31 in different planes by discretising the detector data accordingly and decoding  
 32 each plane, artifacts in the decoded image of one plane typically arise due to  
 33 the presence of sources from other planes. For example Kazachkov et al. [8]  
 34 were able to ascertain the different depths of three point sources by ‘focusing’  
 35 on each plane although the non-focussed sources from the other planes are  
 36 still visible in the form of blurred artifacts. Similarly Mu and Liu were able  
 37 to determine in which of nine planes, each separated by a centimetre, lay two  
 38 extended objects in the shape of a ‘V’ and ‘H’, although again, large artifacts  
 39 remained in the other planes [13].

40 The results in [8] and [13] indicate that further processing of their 3D  
 41 images is possible. Therefore in this article we attempt to achieve this with  
 42 an iterative source removal similar to the CLEAN algorithm used in radio  
 43 astronomy [14].

## 44 2. Coded Aperture Imaging

45 For many practical coded aperture imaging applications, the system often  
 46 chosen is what we term a *perfect* system, namely one where the correlation  
 47 function of the aperture has perfectly flat sidelobes and the shadowgram is  
 48 congruent to a *unit pattern* (also sometimes called the basic pattern) of the  
 49 aperture [3]. Such systems include the uniformly redundant arrays (URA) [3]  
 50 and modified uniformly redundant arrays (MURA) [15]. Note that in far field  
 51 imaging, such as in astronomy, when using a perfect aperture with a detector  
 52 that is the same physical size as the aperture unit pattern, all point sources  
 53 lying in the fully coded field of view (where they project a shadowgram over  
 54 the entire detection plane) will generate a shadowgram that is congruent to  
 55 the aperture unit pattern and so such a system is always perfect. However,  
 56 forming images in the near field will only be perfect for URAs and MURAs  
 57 if all sources being imaged lie in the exact plane that enables these sources  
 58 each to cast a shadow of exactly one unit pattern or its cyclic repetition onto  
 59 the detector. Here we refer to such a plane of a perfect system as the *critical*  
 60 plane. It is evident that only one critical plane exists for a given perfect  
 61 coded aperture system (which for astronomical applications lies at infinity)  
 62 and that these coded aperture systems lose their perfect imaging capability  
 63 when used to observe a scene in which the sources lie at different depths  
 64 because the aperture portions cast by such sources cannot all simultaneously

65 be congruent to the aperture unit pattern. Therefore forming images using  
 66 a coded aperture in the near field presents different problems compared to a  
 67 flat image from sources at large distances.

68 Consider a coded aperture imaging system based on a square geometry  
 69 with an aperture to detector separation of  $s$ . Also consider two point sources  
 70  $\alpha$  and  $\beta$  positioned respectively at depths  $z_\alpha$  and  $z_\beta$  from the detector as  
 71 shown in Fig. 1. Source  $\alpha$  lies at a smaller depth and casts a shadow of  
 72 a portion of the aperture onto the detector. This portion is shown as a  
 73 small square on the aperture and the shadow that it casts is shown on the  
 74 detector. Source  $\beta$  is situated at a larger depth than source  $\alpha$  and it casts  
 75 a shadow of different portion of the aperture, shown as a larger square,  
 76 onto the detector. To avoid confusion, the shadow of  $\beta$  is not shown. The  
 77 closer source casts a smaller aperture portion while at the same time casting  
 78 larger shadows of the individual aperture elements than the further source.  
 79 While the relative sizes of the shadows of the apertures and their elements  
 80 from the different sources allow some depth information to be ascertained,  
 81 in the reconstruction of the final image, sources from one plane are often  
 82 seen as blurred artifacts in the other plane and vice-versa [8]. To decode the  
 83 shadowgram and create a reconstructed image of a plane at depth  $z$ , we can  
 84 adopt the following reasoning. Consider a coded aperture system based on  
 85 a rectangular geometry consisting of a  $(0,1)$  aperture  $A(i,j)$  of dimensions  
 86  $V \times W$  where  $A(i,j) = 1$  for open (transparent) elements and  $A(i,j) = 0$   
 87 for closed (opaque) elements and where  $0 \leq i \leq V - 1$  and  $0 \leq j \leq W - 1$ .  
 88 A number of different aperture configurations exist but for a general system  
 89 using the *balanced decoding* algorithm [3], we have a decoding array  $G(i,j)$   
 90 of the same dimensions as  $A$  where:

$$G(i,j) = 2A(i,j) - 1 \quad (1)$$

91 although slight modifications to Eq. (1) exist for certain types of aperture  
 92 such as the Pseudo-Noise Product Array (PNP) [16] or the MURA arrays  
 93 [15].

94 Assume that we are using a continuous detector, namely one that gives the  
 95 individual detected  $(x,y)$  positions of each photon in list mode. Also consider  
 96 the reconstruction of the image of a 3D field of view (FOV) for a plane at  
 97 depth  $z$  using this detector. Since reconstructing the image requires a cross-  
 98 correlation of the shadowgram with the decoding array [3], it is necessary to  
 99 discretise the detector shadowgram into squares called *bins*, such that each

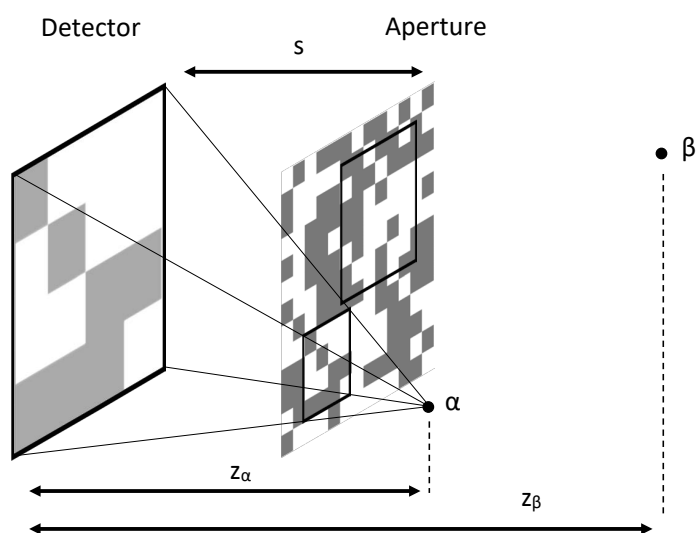


Figure 1: Coded aperture imaging of near field objects.

bin size is the same as that of an aperture element when projected from a point source in the plane at depth  $z$  onto the detector. Therefore the shadowgram is divided into  $v_z \times w_z$  bins and the detected counts within each bin are summed to give a detector array  $P_z(i_z, j_z)$  where  $0 \leq i_z \leq v_z - 1$  and  $0 \leq j_z \leq w_z - 1$ . The  $z$  subscripts are used here to remind us that the various parameters all depend on the plane depth, for example the number of bins  $v_z$  and  $w_z$  both increase with increasing  $z$ .

The decoded image  $I_z(x_z, y_z)$  for the plane at depth  $z$  is calculated as follows:

$$I_z(x_z, y_z) = \sum_{x_z=0}^{v_z-1} \sum_{y_z=0}^{w_z-1} P_z(i_z, j_z) G(i_z + x_z, j_z + y_z) \quad (2)$$

[3]. Each  $(x_z, y_z, z)$  in Eq. (2) can be thought of as a 3D reconstructed object pixel, sometimes also called a *voxel*. Note that since the number of reconstructed voxels at depth  $z$  is given by  $(V - v_z + 1, W - w_z + 1)$  then we have  $0 \leq x_z \leq V - v_z$  and  $0 \leq y_z \leq W - w_z$ . Reconstruction of the image at a given plane at depth  $z$  using Eq. (2) effectively gives an image that is ‘focused’ on that plane. While Eq. (2) provides a method to focus on the different planes of a 3D FOV, sources from one plane typically cause artifacts on other planes in the image leading to overall image degradation. The purpose of this article is to attempt to remove such near field artifacts produced in 3D coded aperture imaging and also determine the actual depth of the source.

Note that in far field imaging such as high energy astronomy, there is only one image plane, lying at infinity, and so there is no image degradation from sources in other planes.

### 3. Image Processing Technique: z-Clean

For the purpose of demonstrating the image processing technique we simulate a prototype coded aperture system having a number of idealised parameters. We assume a continuous square detector of width 30cm having 100% detection efficiency and perfect photon location detection. We employ a non-repeating random pattern for the prototype system aperture and define the square central region of  $v \times v$  elements as the *core* of the aperture with a full aperture of dimension  $2v - 1 \times 2v - 1$  that is not a repeat of the core but instead an array of fully randomised open and closed elements. Note that for a perfect aperture, the core is the unit pattern of the aperture

with size  $v$  and the full aperture is a  $2v - 1 \times 2v - 1$  cyclic repeat of the core. The aperture used for the prototype is the square  $13 \times 13$  element random configuration with a core of  $v = 7$  shown in Fig. 2(a) where the dark and light areas represent the opaque and transparent aperture elements respectively. The aperture elements used in the simulations are of size 2cm, of negligible thickness and with a closed element opacity of 100%. The aperture to detector separation is 30cm. For these parameters the depth of the plane that casts a shadow of the central  $7 \times 7$  aperture elements onto the detector (the equivalent of the critical plane of a perfect system) is 56.25cm from the detector. For this discussion we number the planes in order of  $z$ , with plane 1 being the plane closest to the detector.

For the prototype observation we take the planes as being at 56.25cm (plane 1, also the critical plane), 61.25cm (plane 2) and 66.25cm (plane 3) from the detector and thus we have a total of three planes with a plane separation of 5cm. We assume a single point source situated in plane 2 (61.25cm from the detector) in the centre of the FOV, emitting photons with a detection rate of  $0.01 \text{ cm}^{-2} \text{ s}^{-1}$ . A background rate of  $0.001 \text{ counts cm}^{-2} \text{ s}^{-1}$  is assumed and the observation time is 600s.

The initial shadowgram showing the distribution of counts on the continuous detector is shown in Fig. 2(b) where each point represents the detected position of a photon count. Such location of the individual counts, albeit in practice containing statistical errors, is crucial to the image processing technique. Therefore it is necessary for the data to be in list mode, and note that the shadowgram image in Fig. 2(b) is an unbinned representation of the data in list mode, since individual detected photon positions can be discerned. The central portion of the aperture creating the shadowgram is clearly evident in the distribution of counts shown, with photons from the strong source forming the central pattern of the aperture along with a weaker background. To commence image reconstruction we take each plane and we superimpose the projected bins from these onto the shadowgram. We hereafter refer to the superimposition of bins onto the shadowgram as a *map*. The maps for planes 1 and 2 are shown in the top images in Fig. 3. Note that the map for plane 2 is a good fit with the shadowgram since this plane is where the source is actually located, while the map for plane 1 represents a less good fit with this nearer plane having larger bin sizes. To demonstrate this point more clearly the black square shows in negative the counts corresponding to those photons that passed through a particular open aperture element, namely two elements up and two elements left from the central element. Note that the

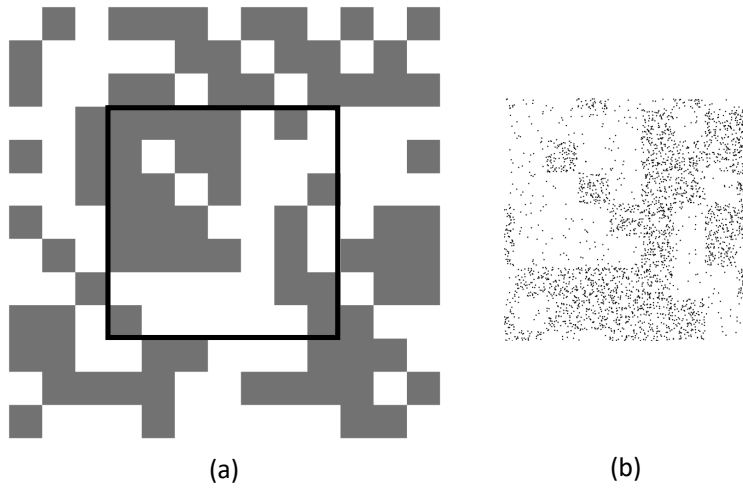


Figure 2: Prototype coded aperture system with (a) random  $13 \times 13$  element coded aperture with the  $v = 7$  element core shown in the central square, (b) continuous detector shadowgram of a single point source in plane 2 at distance  $z = 61.25\text{cm}$  from the detector.



171 black square corresponds exactly with a bin on the map for plane 2 but not  
 172 exactly with a bin of the map for plane 1. A similar situation exists for  
 173 plane 3, but again the fit is not as good as for plane 2, due this time to the  
 174 bins being smaller for plane 3. Binning the shadowgram gives the matrices  
 175 in the lower part of Fig. 3. Using these matrices and decoding each plane  
 176 according to the binning and cross-correlation method outlined in Section 2,  
 177 Eq. (2) we obtain the isometrically projected images in Fig. 4(a). Note that  
 178 the source, which is clearly visible with high intensity at the centre of plane  
 179 2, also appears with somewhat lower intensity at the centres of the other  
 180 planes. Thus we have results similar to those of Kazachkov et al. [8] and  
 181 Mu and Liu [13] inasmuch that sources are ‘blurred’ between planes causing  
 182 artifacts. We now attempt to remove these artifacts in our example.

183 We begin by determining the most likely position of a point source in  
 184 each plane. We do this by performing a simple least-squares fitting of the  
 185 shadowgram with all possible source positions within each plane of the 3D  
 186 FOV, in the form of a  $\chi^2$  minimisation, similar to the method proposed for  
 187 astronomy by Ducros and Ducros [17]. Consider a given plane at depth  $z$ .  
 188 For this analysis we dispense with the  $z$  subscripts, recognising that we are  
 189 working in a given plane at depth  $z$ . For each possible source position  $(x, y)$   
 190 at depth  $z$  we calculate a value of  $\chi^2$  as follows:

$$\chi^2(x, y) = \sum_{i=0}^{V-v} \sum_{j=0}^{W-w} (1/\sigma_{ij}) [P(i, j) - B - S_{xy}A(i + x, j + y)]^2 \quad (3)$$

191 [17, p. 49-50] where  $P(i, j)$  represents the bin counts, examples being the  
 192 matrices in Fig. 3,  $\sigma_{xy}$  is the variance of the counting statistics of  $P$  and  $A$   
 193 is the binary (0, 1) aperture function. The quantities  $S_{xy}$  and  $B$  are numerically  
 194 modelled values, where  $S_{xy}$  represents the intensity per detector bin corre-  
 195 sponding to the open aperture elements at a distance  $z$  from the detector of  
 196 a source situated at a lateral (i.e. the perpendicular direction to  $z$ ) source  
 197 position  $(x, y)$  and  $B$  represents the background noise per detector bin. Note  
 198 that we are here assuming a uniform background of  $B$  which is independent  
 199 of both the source location and detector location. For each possible lateral  
 200 source position  $(x, y)$  we set the partial derivatives of  $\chi^2$  in Eq. (3) with  
 201 respect to  $B$  and  $S_{xy}$  to zero, calculate  $B$  and  $S_{xy}$  from the resulting pair  
 202 of simultaneous equations and then calculate  $\chi^2$  by substituting for  $B$  and  
 203  $S_{xy}$  back into Eq. (3), giving  $\chi^2$  values for each lateral source position  $(x, y)$ .  
 204 Repeating this procedure for all planes gives a 3D matrix of  $\chi^2$  values for

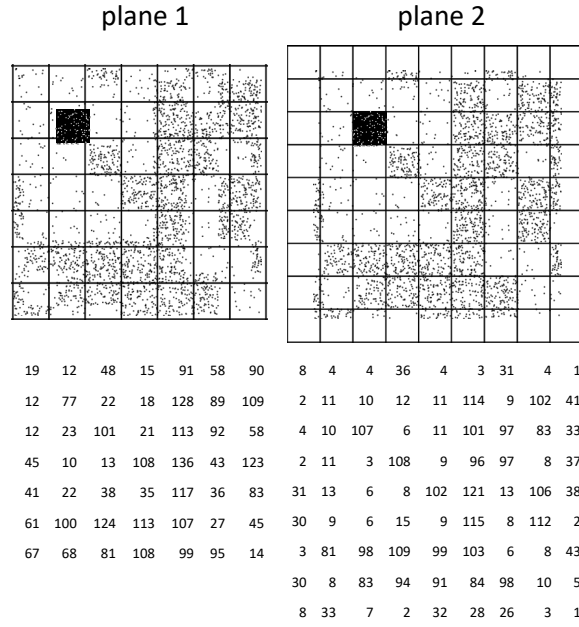


Figure 3: Maps for planes 1 and 2, consisting of bins superimposed on the detector shadowgram. Also shown are the detector image matrices after the counts have been binned.

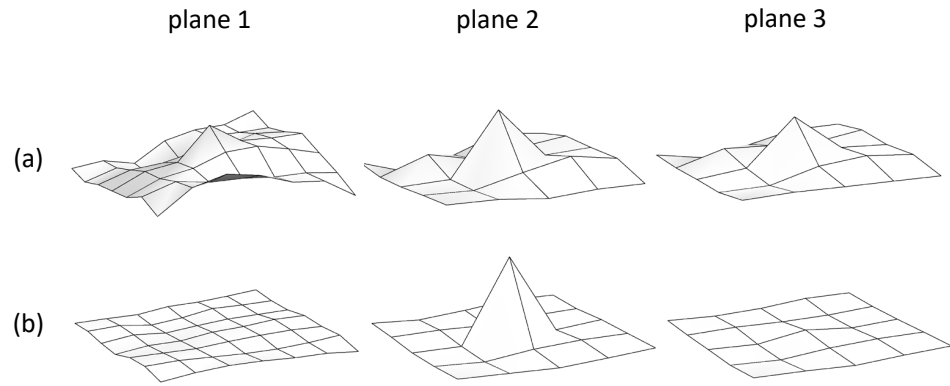


Figure 4: Decoded images for the prototype system for each plane: (a) without z-Clean image processing (b) after the use of z-Clean.

all possible voxel positions  $(x, y, z)$  within the 3D FOV. For example the  $\chi^2$  values for the maps in Fig. 3, for a source in the centre of the FOV of plane 2 are 9.51 for plane 1 and 1.29 for plane 2. The calculation for plane 3 is 2.85. All other possible source positions in the 3D FOV give larger  $\chi^2$  values than these three. The 3D position having the lowest value of  $\chi^2$  is deemed to be the most likely position to contain a point source. We call this point a *candidate* which is in position  $(x_1, y_1, z_1)$  of the 3D reconstructed image. In our example therefore, the map that produces the first candidate is that for the central reconstructed voxel of plane 2. This is because the fit of this particular map is the best. We now process this candidate position by determining for the candidate its value of  $S_{xy}$ , which we now denote by  $S_1$ , and removing from the detector shadowgram  $S_1$  randomly chosen counts from each of the bins of the map for plane 2 in Fig. 3 that correspond to an open aperture element at candidate position  $(x_1, y_1, z_1)$  to give a new shadowgram with fewer counts. An initial 3D matrix  $T(x, y, z)$  with zero-valued elements is defined and the total number of removed counts are then stored and added to cell  $(x_1, y_1, z_1)$  of  $T$  to be used later. The number of counts subtracted from each bin not at the boundary of the map needs to be equal for each corresponding open aperture element, which is  $S_1$ . For an open element bin at the map boundary we subtract the same number of counts but multiplied by the fraction of the bin areas ‘occupied’ by the detector shadowgram in that bin. After subtracting and storing counts, we perform a second iteration of the whole process but this time on the new shadowgram to determine a second candidate with position  $(x_2, y_2, z_2)$  and  $S_{xy} = S_2$ . The corresponding counts are subtracted from the relevant bins of the new shadowgram and added to  $T$ . Note that in different iterations, candidates may coincide but the procedure continues the same. Note also that if there are no counts to subtract from a particular bin then no subtraction takes place from that bin although subtractions from other bins continue. However it is worth noting at this point that the large source and background fluxes used in this study give high detector counts so this situation does not eventuate.

We continue the process until eventually a candidate returns a source intensity  $S_{xy}$  of a negative value which indicates that all possible positive sources have been exhausted. We then perform a cross-correlation of the remaining shadowgrams with the decoding function as per Eq. (2) for each plane and finally we add the data from the matrix  $T$  to the corresponding voxels from the planes of  $I_z$  to produce the final decoded images. Note that this is similar to the technique used to remove artifacts from coded aperture

243 systems having imperfect detectors in [18] and is similar to the CLEAN  
 244 algorithm used in radio astronomy [14] but we here operate in the detector  
 245 shadowgram domain rather than the final reconstructed image domain. For  
 246 ease of discussion we hereafter refer to the whole image processing technique  
 247 as *z-Clean*, with processed images being referred to as having been *z-Cleaned*.

248 In our prototype example the z-Cleaned images are shown in Fig. 4(b).  
 249 We can see that the reconstructed source position is clearly visible in plane  
 250 2, the actual plane containing the source, while the artifacts in the other  
 251 planes have been largely removed although some minor ‘ghosting’ can be  
 252 seen in the central pixel of plane 3. Note also that the z-Clean technique has  
 253 the added benefit of removing much of the noise produced by the random  
 254 nature of the coded aperture, with the processed images in Fig. 4(b) having  
 255 flatter sidelobes than those in Fig. 4(a). This is to be expected, since the  
 256 CLEAN algorithm is capable of removing a range of significant artifacts,  
 257 which includes those caused by the random noise produced when using a  
 258 coded aperture that does not have perfect imaging capability, such as the  
 259 random aperture used in the prototype.

260 We conclude this section by commenting on the point that in coded aper-  
 261 ture imaging, cleaning can be accomplished either by operating in the 2D  
 262 shadowgram domain, and subtracting individual photon counts from the de-  
 263 tector, or operating in the 3D reconstructed image domain and subtracting  
 264 spurious peaks from each of the planes being studied. We here adopt the  
 265 approach of subtracting from the 2D detector domain as it is much simpler  
 266 than the complex computation when operating in the 3D domain.

## 267 4. Computer Simulations

268 Computer simulations were conducted to test the z-Clean technique de-  
 269 scribed in Section 3 when using two types of high energy photon detector: a  
 270 continuous detector and a pixellated detector. It is evident that a continu-  
 271 ous detector is a certain type of idealised detector inasmuch that data can  
 272 be acquired in list mode and hence affords the user the opportunity to define  
 273 the bin size according to a particular plane depth being studied. However in  
 274 practice, detectors are often not continuous but are instead pixellated. For  
 275 example 0.2cm pixels are typical for cadmium zinc telluride detectors. There-  
 276 fore for most applications it is also necessary to assess the z-Clean technique  
 277 when used with a pixellated detector.

For both types of detector, a number of assumptions are made when performing the simulations, including a few idealisations. For the continuous detector, staff at Auckland Hospital were consulted as to the expected performance of such a detector system when using a coded aperture. As a result of these discussions, the continuous detector simulated is a square 35cm by 35cm plate, possessing a photon location accuracy that has a Gaussian profile with a full width at half maximum (FWHM) of 1cm. For the pixellated detector we employ 0.2cm pixels which, assuming a 35cm  $\times$  35cm detector (or an array of smaller detectors with a total size of 35cm  $\times$  35cm) gives a detector with 175  $\times$  175 pixels. The pixellated detector is assumed to have the capability of rejecting simultaneous multi-site events and hence able, for example, to reject any photons that undergo Compton scattering that deposits energy in more than one pixel. For both detectors a photon detection efficiency of 70% is assumed.

For both the continuous and pixellated detectors systems, the aperture pattern chosen is a square MURA with unit pattern (or core) of size  $v = 31$ , cyclically repeated to give an overall aperture of size  $61 \times 61$  elements (namely  $2v - 1 \times 2v - 1$ ) and 50% throughput shown in Fig. 5. Past research by Fenimore [19] and by in't Zand et al. [20] into optimum aperture throughput show that, while values other than 50% may be best for certain source fields, a 50% throughput still gives very good results for point source observations. Furthermore, as the purpose of this study is to demonstrate the efficacy of z-Clean, we here use the more well-known MURA aperture for simplicity and familiarity while recognising that testing z-Clean with different aperture types is a possible area for further research that is beyond the scope of this study. The aperture to detector separation is set at 30cm and aperture elements of size 0.6cm are chosen giving an overall aperture size of 36.6cm. The reason for choosing this aperture element size is that it means that the projected aperture elements from sources in the FOV onto the detector are of the order of the FWHM of the continuous detector. Perfectly square aperture elements of negligible thickness are assumed with a closed element opacity of 99%. A uniform detector background of one count  $\text{cm}^{-2} \text{s}^{-1}$  is assumed. Observation time is 600s.

For all simulated observations, a field with four point sources of different intensities is chosen. The first is of activity 100kBq situated at a depth of 72cm from the detector and lying in the centre of the FOV, the second is of activity 50kBq at a depth of 74.7cm and lying to the left of the central source, the third is 10kBq at 69.5cm, lying to the right of the central source

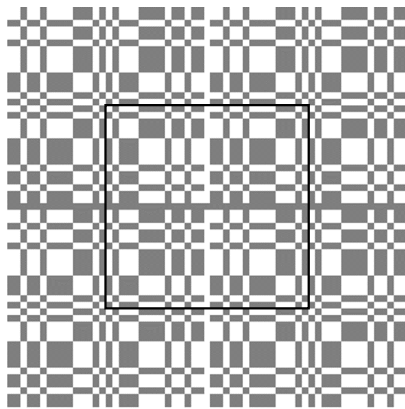


Figure 5: MURA coded aperture of  $v = 31$  and overall size  $61 \times 61$  used in the simulations of Sections 5 and 6. The central  $v \times v$  unit pattern, or core, is also shown inside the black edged square.

316 and the fourth is 5kBq at 71cm lying roughly halfway between the centre and  
 317 the lower left corner of the FOV (see also Fig. 6). These source parameters  
 318 are chosen to demonstrate the efficacy of the z-Clean technique when both  
 319 weak and strong sources are present, lying at depths representing exactly  
 320 those in a plane to be decoded and also between planes to be decoded. All  
 321 sources are assumed to be in the very centre of a voxel in the lateral  $(x, y)$   
 322 direction, which for data in list mode is always possible as we can define our  
 323 own detector bins without any great loss of generality. For each observation  
 324 twenty trials are conducted to give an indication of the spread of the signal  
 325 to noise ratio (SNR) values of the individual sources. We present results of  
 326 four point sources only, since results for fewer sources are at least as good  
 327 and in many cases marginally better than the results for four sources. The  
 328 quality of the resulting z-Cleaned images is also compared to those produced  
 329 by twenty trials of a perfect coded aperture system operating only in its  
 330 critical plane and hence not affected by depth effects.

331 Once the detector data is collected the z-Clean technique is applied be-  
 332 tween the minimum and maximum depths of 66cm and 78cm respectively.  
 333 For each observation the shadowgram is decoded for a range of plane separa-  
 334 tions with planes being equally separated in each case. We test the technique  
 335 for plane separations of 2cm (giving 7 planes from 66cm to 78cm), 1cm (13  
 336 planes), 0.5cm (25 planes) and 0.1cm (121 planes). In all cases the central  
 337 plane lies at a depth of 72cm.

338 As noted, the results and SNR values of the sources are compared to  
 339 those expected for a perfect imaging system operating only in its critical  
 340 plane. For this we use the same  $31 \times 31$  element MURA. Because perfect  
 341 imaging for MURA arrays requires the source to lie in the critical plane,  
 342 we adopt the following approach to obtain correct SNR values for a point  
 343 source at a given depth. Employing the  $31 \times 31$  element MURA aperture  
 344 we use the same system parameters as per the z-Cleaned image observations  
 345 except that we adjust the aperture to detector separation so as to place the  
 346 point source in the critical plane, where the source now casts a shadow of  
 347 exactly a full unit pattern of the aperture onto the detector. Then we make  
 348 an observation of this single source, ensuring that we adjust the background  
 349 level to take account of the extra statistics produced by the presence of the  
 350 other sources at other depths but not modulated by the aperture, and decode  
 351 using Eq. (2) (note that we do not process this image any further as we  
 352 wish to compare our z-Cleaned images with a single decoded image of a  
 353 perfect system that suffers no degradation from depth effects). Thus we are



354 comparing our simulated observation results to a genuinely perfect coded  
 355 aperture system that is observing a single source, with corrected statistics  
 356 for other sources unmodulated by the aperture. Again we perform twenty  
 357 repeated trials of each critical plane observation.

## 358 5. Continuous Detector Results

359 Images for a typical observation using the continuous detector are shown  
 360 in Fig. 6. Presented in this figure are the unprocessed and z-Cleaned images  
 361 for a plane separation of 2cm, and z-Cleaned images for 1cm plane separation.  
 362 Although more planes than these were processed, only those planes from  
 363 depths 70cm to 78cm are shown as there were no noticeable artifacts in the  
 364 z-Cleaned images for planes outside this range.

365 For the unprocessed images at 2cm plane separation large artifacts, sim-  
 366 ilar to those in Fig. 4(a), are present in all planes in the form of repetitions  
 367 of the 100kBq source at the centre of the FOV and of the 50kBq source left  
 368 of the centre of the FOV. The 10kBq source and repeated artifacts are just  
 369 visible to the right of the centre of the FOV at depths of 70cm, 72cm and  
 370 74cm. As a result of the large artifacts it is difficult to ascertain the true  
 371 depths of these sources. However, the z-Cleaned images for a plane separa-  
 372 tion of 2cm demonstrate the efficacy of the z-Clean technique, inasmuch that  
 373 the large artifacts that recur in all planes of the unprocessed images have  
 374 been largely removed from the planes where the sources are not present,  
 375 to leave the true sources clearly visible with only minor ghosting in other  
 376 planes. We here make the distinction that an artifact is a repeat of a source  
 377 appearing in a different plane to the actual source for an unprocessed image  
 378 and a ghost is such a repeat but in an image that has been processed by  
 379 the use of z-Clean. Typically the ghosts are much smaller than the artifacts.  
 380 The central 100kBq source is clearly reconstructed at its correct depth of  
 381 72cm and has also been successfully z-Cleaned, with only minor ghosting of  
 382 this source in the adjacent planes at 70cm and 74cm, as would be expected  
 383 given the imperfect photon position location capability of the detector. The  
 384 50kBq source has also been successfully z-Cleaned and the reconstructed flux  
 385 of this source, which is actually positioned at a depth of 74.7cm is shared  
 386 in roughly correct proportions between the planes either side of this depth,  
 387 namely there is a large peak in the closest plane at 74cm and a smaller peak  
 388 in the more distant plane at 76cm. The phenomenon of a single source being  
 389 shared over more than a single pixel, or in this case a voxel, is also known as

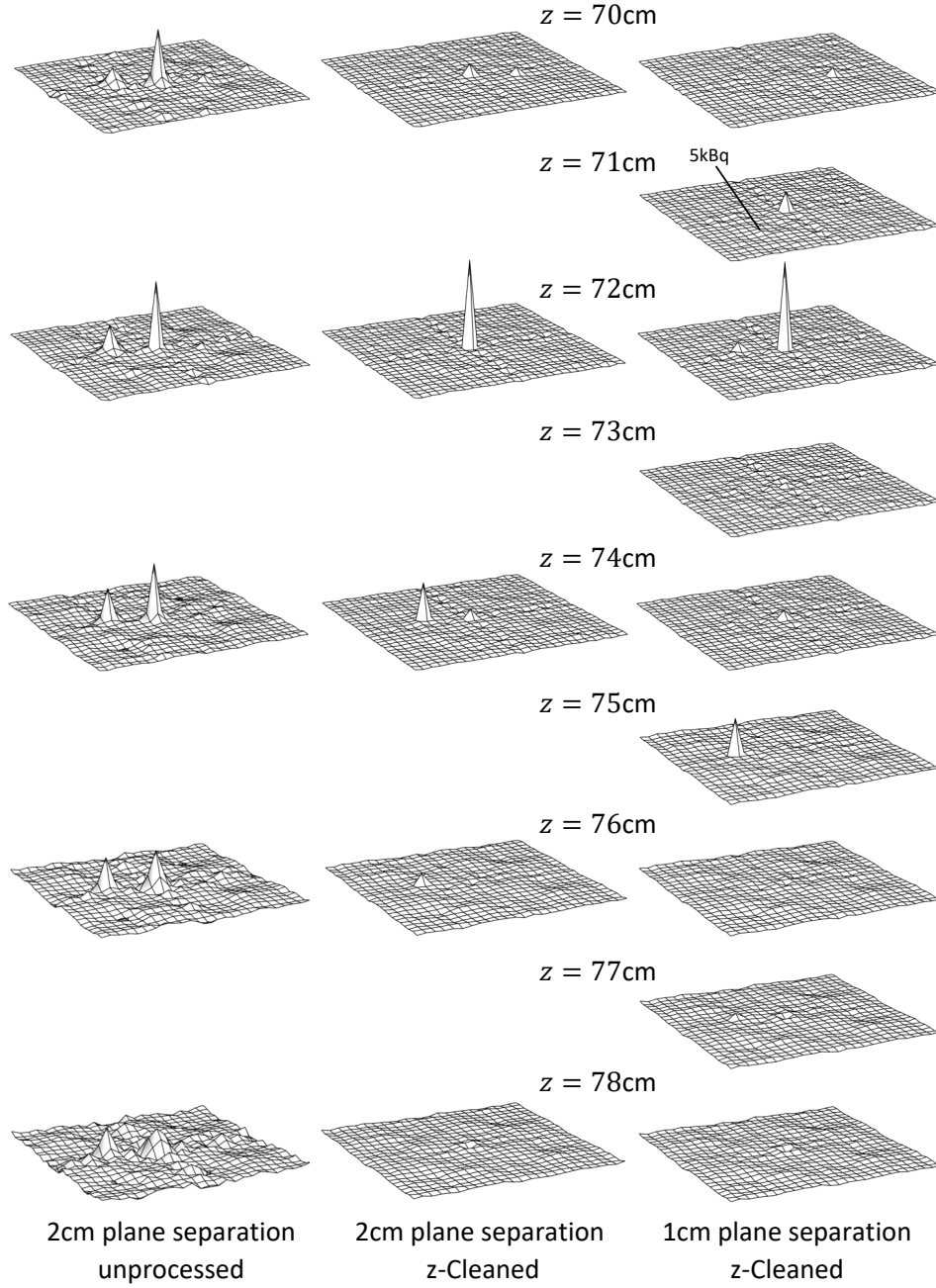


Figure 6: Typical images for simulations using z-Clean for 2cm and 1cm plane separations for the continuous detector.

390 a *phasing error* [21] and has been discussed in the literature for sources lying  
 391 close to object pixel boundaries in the  $(x, y)$  directions [22]. In this case we  
 392 have similar phasing error occurring but this time over more than one voxel  
 393 in the  $z$  direction. We hereafter refer to this phenomenon, when it occurs, as  
 394 *phasing*. The 10kBq source lying at 69.5cm is reconstructed and successfully  
 395 z-Cleaned and appears in its closest plane at 70cm although there was no  
 396 apparent phasing of this source in the 68cm plane. The 5kBq source lying  
 397 at a depth of 71cm (indicated in Fig. 6 at 1cm plane separation) is barely  
 398 visible at 2cm plane separation at depths of 70cm and 72cm.

399 For 1cm plane separation, the central 100kBq source has been successfully  
 400 z-Cleaned although there is ghosting in the adjacent plane at 71cm and also  
 401 two planes away at 74cm, the 50kBq source is reconstructed entirely at its  
 402 closest plane of 75cm with no significant phasing of the source at 74cm, but  
 403 with ghosting at 77cm, and the 10kBq source at 69.5cm depth is visible in  
 404 the plane at 70cm but there was no ghosting or phasing of this source in any  
 405 of the other planes. The 5kBq source that lies at 71cm depth is indicated  
 406 and is only just visible in the plane at this depth. However, close inspection  
 407 of the images reveals artifacts of this source of approximately the same size  
 408 also appearing in the planes at depths of 70cm and 72cm, indicating that no  
 409 z-Cleaning of this source has taken place.

410 The results in Fig. 6 represent a single typical observation for plane separa-  
 411 tions of 2cm and 1cm. However for each observation twenty trials were car-  
 412 ried out and more detailed results from these for the three strongest sources  
 413 are shown in Fig. 7 and Tables 1 and 2. Data for the 5kBq source is not in-  
 414 cluded in the tables because there was no successful z-Cleaning of this source  
 415 and hence no method of determining the parameters for the tables. Fig. 7  
 416 shows some SNR depth profiles for the three strongest reconstructed sources  
 417 at plane separations of 2cm and 1cm, as well as for the finer depth resolutions  
 418 of 0.5cm and 0.1cm. Here, and for all later observations to follow, each graph  
 419 shows profiles judiciously chosen to demonstrate a typical range of outcomes  
 420 for each case. In some cases either two or three of each of the twenty trials  
 421 are shown while for those cases where all trials, or a large majority of trials  
 422 (eighteen or nineteen) follow a particular profile, the mean profile is plotted  
 423 and marked with disks at the graph vertices. The number of such trials is  
 424 labelled appropriately on the relevant graphs. In these cases the standard  
 425 error in the mean was also calculated, although it is worth stating at this  
 426 point that for all such profiles shown, the resulting error bars are smaller  
 427 than the disks on the graphs.

Table 1: SNR, reconstructed depth ( $z$ ) and  $\text{PSLA}_z$  results obtained for twenty trials of the continuous detector for the three strongest sources. For those values without errors quoted, the error is less than 0.001.

|                        | 100kBq at 72cm   | 50kBq at 74.7cm  | 10kBq at 69.5cm   |
|------------------------|------------------|------------------|-------------------|
| Critical plane SNR     | $111.7 \pm 0.3$  | $78.8 \pm 0.4$   | $22.0 \pm 0.2$    |
| 2cm plane separation   |                  |                  |                   |
| SNR                    | $131.7 \pm 0.5$  | $56.0 \pm 0.5$   | $11.3 \pm 0.1$    |
| $z$ (cm)               | $71.93 \pm 0.01$ | $74.52 \pm 0.02$ | $69.87 \pm 0.02$  |
| $\text{PSLA}_z$ (cm)   | 0.021            | 0.051            | $0.250 \pm 0.003$ |
| 1cm plane separation   |                  |                  |                   |
| SNR                    | $125.5 \pm 0.5$  | $50.3 \pm 0.5$   | $11.6 \pm 0.2$    |
| $z$ (cm)               | $71.99 \pm 0.02$ | $74.81 \pm 0.07$ | $69.45 \pm 0.10$  |
| $\text{PSLA}_z$ (cm)   | 0.011            | 0.028            | $0.122 \pm 0.002$ |
| 0.5cm plane separation |                  |                  |                   |
| SNR                    | $125.9 \pm 1.0$  | $50.0 \pm 0.6$   | $11.6 \pm 0.2$    |
| $z$ (cm)               | $72.02 \pm 0.01$ | $74.46 \pm 0.04$ | $69.47 \pm 0.06$  |
| $\text{PSLA}_z$ (cm)   | 0.006            | 0.014            | $0.061 \pm 0.001$ |
| 0.1cm plane separation |                  |                  |                   |
| SNR                    | $112.7 \pm 1.3$  | $49.0 \pm 0.5$   | $11.3 \pm 0.2$    |
| $z$ (cm)               | $71.95 \pm 0.02$ | $74.60 \pm 0.04$ | $69.47 \pm 0.05$  |
| $\text{PSLA}_z$ (cm)   | 0.001            | 0.003            | 0.012             |

Table 1 presents the reconstructed SNR values for the three strongest sources, as well as the mean SNR for twenty trials of the same source operating in the critical plane. The table also shows depth calculations and the point source location accuracies ( $\text{PSLA}$ ) in the depth direction,  $\text{PSLA}_z$ . All quantities are shown with standard errors in the means, unless the errors are very small in which case no errors are reported. For sources that are shared between planes with a phasing error, the SNR for each trial is calculated in quadrature from the two planes containing the source, with statistics calculated from the twenty different SNR values from all trials. Reconstructed source depths are calculated separately for each trial by Gaussian fitting to these individual profiles, and then mean depths with statistics are obtained from the twenty trials.

$\text{PSLA}_z$  has also been estimated from the results and is also presented in Table 1. The  $\text{PSLA}$  of a coded aperture imaging system is dependent upon the source SNR. For a perfect coded aperture system operating only in its

Table 2: Continuous detector: furthest distances of main reconstructed peaks from the actual source depth of twenty trials for each observation of the three strongest sources. All values are in cm. Asterisks denote actual source not lying at a plane to be decoded.

| Plane separation | Source         |                 |                 |
|------------------|----------------|-----------------|-----------------|
|                  | 100kBq at 72cm | 50kBq at 74.7cm | 10kBq at 69.5cm |
| 2                | 0              | 0.7*            | 0.5*            |
| 1                | 0              | 0.7*            | 0.5*            |
| 0.5              | 0              | 0.7*            | 0.5             |
| 0.1              | 0.2            | 0.4             | 0.5             |

critical plane, the 2D PSLA in the  $(x, y)$  plane can be calculated using the results of Skinner [23] and is given by  $\text{PSLA} = s \times d\alpha$  where  $s$  is the aperture to detector separation and  $d\alpha$  is the PSLA in radians. Using [23] Eq. (31) and assuming aperture elements and detector pixels of size  $m$  we have

$$\text{PSLA} = \frac{s}{\text{SNR}} k[2(m/s)^2]^{1/2} \quad (4)$$

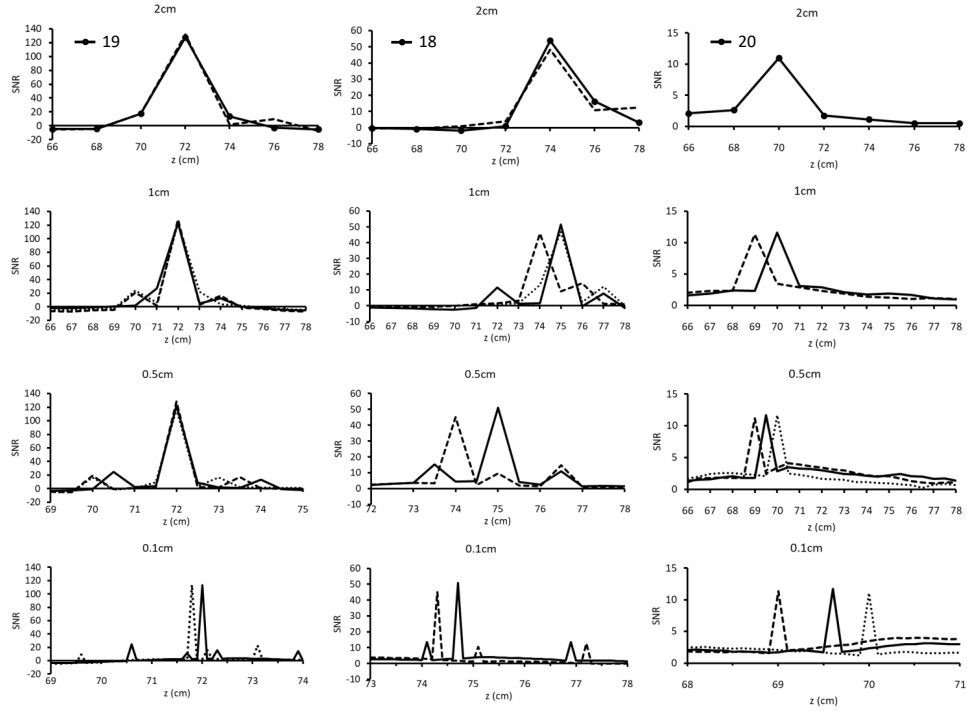
where  $k \simeq 1$  is Skinner's constant. Now, in the  $z$  direction, calculating the PSLA, which we denote  $\text{PSLA}_z$ , is directly analogous to Skinner's analysis. Instead of a pixel of size  $m$  in the  $(x, y)$  plane we have a voxel of size  $d$  in the  $z$  direction. Substituting this with  $k = 1$  into Eq. (4) and simplifying gives

$$\text{PSLA}_z = \frac{1.4d}{\text{SNR}}. \quad (5)$$

The results for the continuous detector are now discussed.

### 5.1. Continuous Detector - Depth Profiles

For the 100kBq source at 2cm plane separation (top graph in Fig. 7(a)) two SNR depth profiles are shown. The dark line represents the mean profile of nineteen trials (denoted by the key in the corner of the graph) that all follow this same general profile. As stated above, the error bars to represent standard errors in the means are smaller than the disks at the profile vertices. This mean profile shows a clear peak at the actual source depth of 72cm, but with ghosts appearing in the adjacent planes at depths of 70cm and 74cm. The remaining trial gives the dashed profile on the graph, which shows the reconstructed source peak correctly positioned at 72cm and with a ghost in the adjacent plane at 70cm, but also a ghost situated on the opposite



(a) 100kBq at 72cm

(b) 50kBq at 74.7cm

(c) 10kBq at 69.5cm

Figure 7: Selected examples of SNR depth profiles of the three strongest sources using a continuous detector. The graph titles show the plane separations.

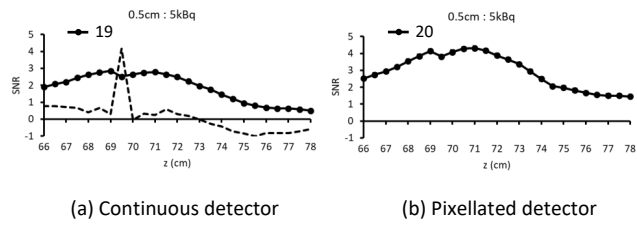


Figure 8: Profiles for the 5kBq source at 71cm depth using 0.5cm plane separation for both detector types.

463 side of the peak at 76cm depth, which is two planes away from the main  
 464 peak. Therefore for all twenty trials the main reconstructed peak appears at  
 465 the correct depth of the source, namely 72cm, although there is a very small  
 466 amount of variation in the positions of ghosts. For the 100kBq source at both  
 467 1cm and 0.5cm plane separations, Fig. 7(a) shows three profiles in each case,  
 468 one for each of three selected trials, and all producing reconstructed source  
 469 peaks at the correct depth of 72cm. However, ghosts of differing sizes appear  
 470 at varying depths, being separated from the main peak by a combination of  
 471 one and/or two planes for 1cm separation and up to four planes for 0.5cm  
 472 separation, to give a range of differing profiles. The appearance of ghosts  
 473 at different depths for different trials indicates that their occurrence is not  
 474 purely systematic but contains a random component. For both of these  
 475 plane separations, the results represent a blurring of up to around 2cm from  
 476 the main reconstructed peak. As is the case for 2cm plane separation, all  
 477 trials reconstruct the main peak in the correct position at 72cm depth. For  
 478 0.1cm plane separation, Fig. 6 shows profiles for two trials, where the main  
 479 reconstructed peaks appear at different depths for the different trials, one  
 480 in the correct position at 72cm and the other at 71.8cm. It is because not  
 481 all of the reconstructed main peaks appear in the same plane that no finer  
 482 plane separation than 0.1cm was studied for the continuous detector. Both of  
 483 the profiles for 0.1cm plane separation present non-systematic ghosts either  
 484 side of and up to approximately 2cm away from the main peaks. Again,  
 485 the variation in the positions of the ghosts for different trials indicates that  
 486 their appearance in the z-Clean process is not systematic. Table 2 shows the  
 487 furthest distance in the  $z$  direction for the twenty trials of each observation  
 488 of any of the main reconstructed peaks from the actual source depth. The  
 489 results for all three plane separations of 2cm, 1cm and 0.5cm have all twenty  
 490 trials reconstructing the main peak of the 100kBq source at 72cm, and hence  
 491 a furthest distance of 0cm from the actual source depth, as per Table 2. For  
 492 0.1cm plane separation the furthest distance of a main peak from the actual  
 493 source position is 0.2cm.

494 Profiles for the 50kBq source located at 74.7cm depth are shown in Fig.  
 495 7(b). For 2cm plane separation, eighteen trials give a profile similar to the  
 496 dark line (top graph). The phasing is evident in the sharing of the recon-  
 497 structed source flux over two planes, namely 74cm and 76cm, as to be ex-  
 498 pected from the source depth of 74.7cm. The remaining two trials give profiles  
 499 similar to the dashed line. Unlike the case for the 100kBq source, for the  
 500 finer plane separations of 1cm, 0.5cm and 0.1cm the reconstructed peaks for



different trials do not all appear at the same depth, as shown in the profiles, three of which are shown for 1cm plane separation and two each for 0.5cm and 0.1cm plane separations. However, for all trials of this source at 0.5cm and 0.1cm plane separations, the main reconstructed peaks appear no further than 0.7cm and 0.4cm from the actual source depth respectively (Table 2). Once again, the appearance of ghosts either side of each main peak is not systematic and seems to represent an overall blurring of around 2cm to 3cm either side of the main peaks.

For the twenty trials of the 10kBq source for 2cm plane separation, every trial follows the same profile as the top graph in Fig. 7(c). The main peak is reconstructed at 70cm, which is 0.5cm from the actual source depth. The voxels either side of the main peak are below the  $3\sigma$  threshold so there is no obvious phasing of this source from the main reconstructed peak. For 1cm plane separation for this source, the twenty trials follow either one of the two profiles shown in the second graph in Fig. 7(c), with peaks appearing at either 69cm or 70cm depth, thus being no further than 0.5cm from the actual source depth. For the finer plane separations of 0.5cm and 0.1cm, the reconstructed peaks also do not all appear at the same depth, although for all trials of the 10kBq source, these peaks appear no further than 0.5cm from the actual source depth for all plane separations. Furthermore, unlike the two stronger sources, no ghosts appear in the profiles. This is due to the fact that no candidates at depths other than the main peak are obtained, probably as a result of the weak nature of the 10kBq source which is less likely to contribute candidates in more than one iteration of the z-Clean process while in the presence of other stronger sources and a high background level. The z-Cleaning of the three strongest sources to remove large artifacts and leave only a small level of minor ghosting demonstrates the efficacy of the z-Clean technique for these three sources.

As mentioned earlier, the 5kBq source is barely visible and does not appear to have been z-Cleaned. In Fig. 8(a) the dark line shows the mean profile of nineteen trials for the 5kBq source at 0.5cm plane separation using the continuous detector, indicating that for all of these trials the SNR barely reaches 3 at around the actual source depth. There is no reconstructed peak, and hence no z-Cleaning of the images for these trials. Note that this result is also consistent with the 1cm plane separation images of Fig. 6 for which z-Clean also did not remove the artifacts. However, one trial gives the dashed profile, with a clearly reconstructed peak at 69.5cm depth, namely 1.5cm from the actual source depth of 71cm, and lower sidelobes, indicating that z-

539 Clean has taken place but giving a less accurate reconstructed peak location  
540 than for the three stronger sources. For the other plane separations we do  
541 not present results since the profiles obtained for all trials of the 5kBq source  
542 were similar to those of the dark line in Fig. 6, indicating no z-Cleaning for  
543 these cases. This would suggest that for the parameters studied, successful  
544 z-Cleaning of a 5kBq source for a given observation would only occur very  
545 rarely.

### 546 5.2. Continuous Detector - Reconstructed Source Depths

547 While Table 2 gives the furthest reconstruction of a peak from the ac-  
548 tual source depth, Gaussian fitting of the data allows more accurate source  
549 depth information to be determined. For each trial, the data was fitted to  
550 a Gaussian distribution for each of the three strongest sources to determine  
551 source depth for each trial and the statistical data was then calculated from  
552 the twenty trials. The results are given in Table 1.

553 The depth location is very good in all cases for the three strongest sources  
554 for all plane separations, with the values all being compatible with the ac-  
555 tual depths of the three sources in all cases. In general the sources that  
556 suffer a phasing error are located with lower precision, namely the 50kBq  
557 source using 2cm, 1cm and 0.5cm plane separations for which reconstructed  
558 source depths were 0.18cm, 0.11cm and 0.24cm from the actual source depth  
559 respectively, and the 10kBq source at 2cm and 1cm plane separations for  
560 which reconstructed source depths are respectively 0.37cm and 0.05cm from  
561 the actual source depths. For all other source observations at other plane  
562 separations, where there is no phasing error, the reconstructed source depths  
563 are generally better, ranging from around 0.1cm from the actual source depth  
564 for many cases to only 0.01cm from the actual source depth in the case of the  
565 100kBq source at 1cm plane separation. For all cases of the three strongest  
566 sources the depth location is very good although, outside of a phasing error  
567 discrepancy, there is no clear systematic pattern in the ability to reconstruct  
568 a source at the correct depth.

### 569 5.3. Continuous Detector - SNR and $PSLA_z$

570 The SNR data for the reconstructed 100kBq, 50kBq and 10kBq sources  
571 using all plane separations is given in Table 1, along with values for the  
572 critical plane observations. For the 100kBq source the reconstructed SNR  
573 for all plane separations unexpectedly exceeds the value for the critical plane  
574 observations. The reason for this is explained as follows. For observations

at the critical plane, a reconstructed source peak comes with a number of  
 smaller ghosts either side and adjacent to the central peak, typically four to  
 eight in a cross or a square formation, due to a blurring that is typical of the  
 coded aperture imaging technique. These artifacts increase the variability of  
 the sidelobes around the reconstructed source peak and lead to a reduction  
 in the reconstructed source SNR. Now, in the iterative z-Clean process, the  
 first candidate for the strong 100kBq source is correctly chosen in the central  
 $(x, y)$  voxel and at a depth of 72cm for which counts are then subtracted and  
 stored appropriately for later use. However, the second candidate chosen for  
 this source is typically not located in a voxel at the same depth and adjacent  
 to the main peak, but instead is located in the same  $(x, y)$  position but at a  
 different depth, an example being at 70cm depth for the 2cm plane separation  
 images and appearing as a ghost in Fig. 6. When counts are removed for this  
 incorrectly-located ghost candidate, it also singularly removes counts that  
 would otherwise have been allocated to a number of sidelobe candidates  
 that would have appeared at 72cm depth and adjacent to the main peak,  
 had the second candidate not already have been assigned these counts, thus  
 suppressing the sidelobes and reducing the overall variability of the image,  
 and hence artificially increasing the SNR of the main reconstructed peak.  
 Note for the particular case of Fig. 6, the effect is compounded by a further  
 ghost located in the same  $(x, y)$  position but at 74cm depth. For 2cm plane  
 separation the effect here is to reduce the noise by approximately 18% and  
 increase the SNR from 117 to 131. Note that for weaker sources, this effect  
 is less marked as here the detector background has the more dominant effect  
 than the location of incorrect candidates on the overall variability. The SNR  
 of the 100kBq source reduces slightly as the plane separation becomes finer,  
 from  $131.7 \pm 0.5$  at 2cm plane separation to  $112.7 \pm 1.3$  at 0.1cm plane  
 separation. As a result of the unexpected increase in the SNR for this strong  
 source, the  $\text{PSLA}_z$  values for this source need to be taken with some level of  
 caution, and in reality the quantities are probably more accurately reflected  
 by using the critical plane SNR value of 111.7 in Eq. (5). Using this value  
 gives  $\text{PSLA}_z$  values of 0.025cm, 0.013cm, 0.006cm and 0.001cm for plane  
 separations of 2cm, 1cm, 0.5cm and 0.1cm respectively.

For the 50kBq source, there is a clear phasing for 2cm plane separation  
 over the two planes at depths of 74cm and 76cm. Therefore the SNR values  
 for this source are calculated in quadrature over these two planes for each of  
 the twenty trials individually and the results are combined to give the mean  
 and standard error in the mean in Table 1. The results indicate a reduction

in SNR compared to that of the critical plane observation that increases with decreasing plane separation, ranging from 29% for 2cm plane separation, up to 38% for 0.1cm plane separation.

For the 10kBq source, the SNR similarly suffers a reduction compared to the critical plane, which is more severe compared to that for the 50kBq source, being around 47% to 49%. However, the reconstructed SNR is much more consistent for the 10kBq source across different planes, with very little variation.

As already noted,  $PSLA_z$  depends on SNR and plane separation, generally improving with increased SNR and with finer plane separation. For the 100kBq source  $PSLA_z$  ranges from 0.021cm for 2cm plane separation to 0.001cm for 0.1cm plane separation, for the 50kBq source from 0.051cm at 2cm plane separation to 0.003cm at 0.1cm plane separation, and for the 10kBq from 0.250cm at 2cm plane separation to 0.012cm at 0.1cm plane separation.

## 6. Pixellated Detector Results

As noted in Section 4, the use of the chosen pixellated detector means that the data collected comes as a  $175 \times 175$  matrix of counts. However, the z-Clean technique requires data to be in list mode, namely having actual positions of individual detected photons, so that the counts can be binned and z-Cleaned according to which plane is being studied at any particular time. Therefore to replicate a list mode output, each detected count within a detector pixel is randomly allocated an  $(x, y)$  coordinate within that pixel on the detector so that rather than having a matrix of counts, we instead have a list of  $(x, y)$  detector coordinates as though the data were in list mode. We then proceed with the z-Clean technique as explained in Section 3. In the following we present results of simulations described in Section 4.

The z-Cleaned images of a typical observation for each of the plane separations of 2cm and 1cm are shown in Fig. 9. As for the continuous detector images, only planes from depths 70cm to 78cm are shown as there were no noticeable ghosts in the planes outside this range. The images in Fig. 9 are similar to those for the continuous detector in that the three strongest sources are all clearly visible and have largely been successfully z-Cleaned, with only minor ghosting in some nearby planes.

At 2cm plane separation, the 100kBq source is reconstructed at the actual source depth of 72cm with a ghost at 70cm although, unlike the case for the

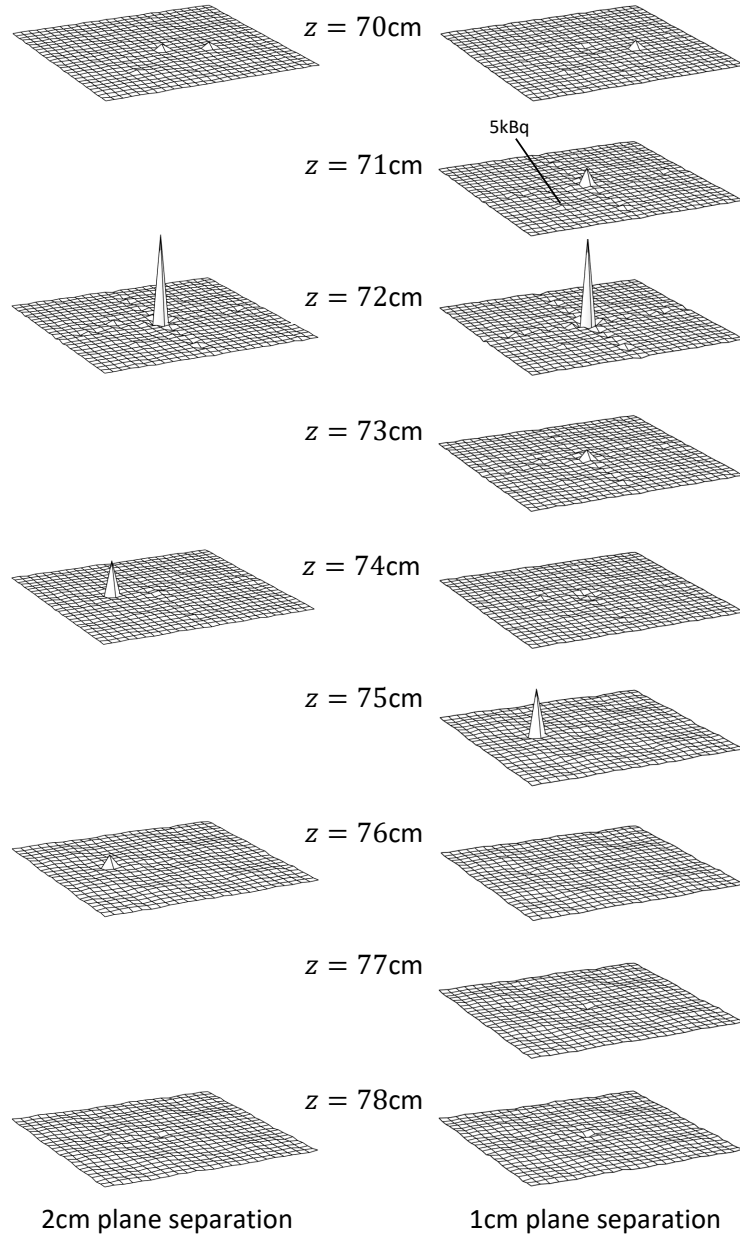


Figure 9: Typical images for simulations using z-Clean for 2cm and 1cm plane separations for the pixellated detector.

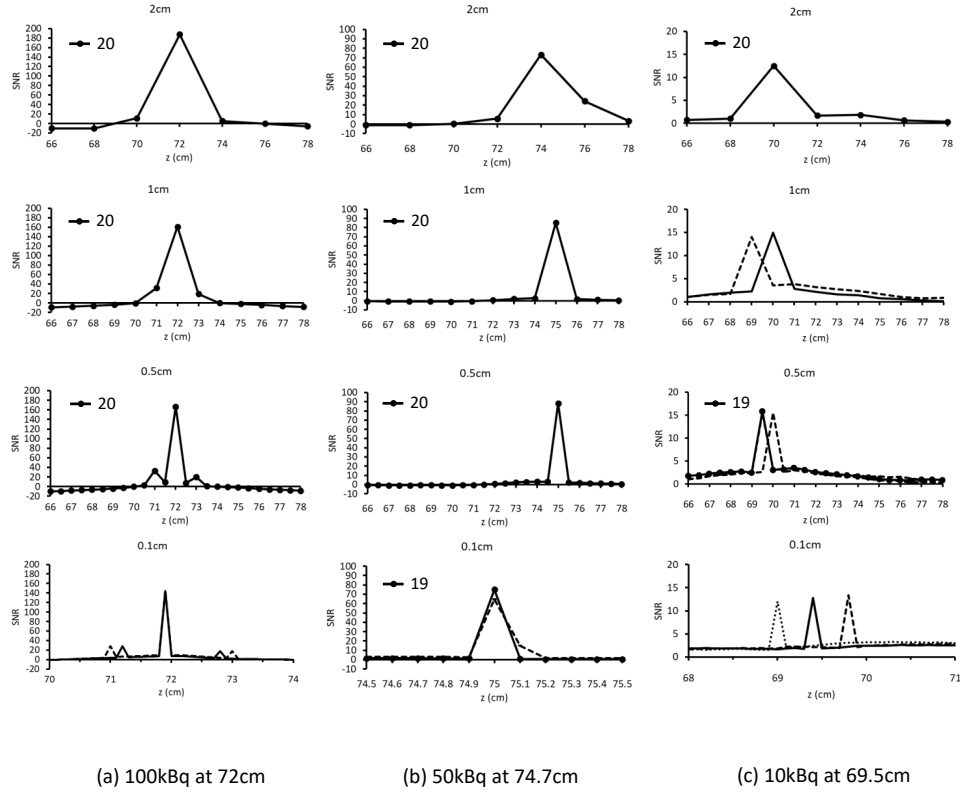
continuous detector, there is no significant ghosting at 74cm. The 50kBq source at 74.7cm depth is again proportionately shared between two planes as a phasing error at depths of 74cm and 76cm, with no ghosting in any other plane, and the 10kBq source at 69.5cm depth is visible at 70cm with no phasing or ghosting evident in any other plane. The 5kBq source at 71cm depth is just discernable in the planes at 70cm, 72cm and possibly even at 74cm, with no apparent z-Cleaning of this source having taken place.

At 1cm plane separation the 100kBq source is clearly reconstructed at its correct depth of 72cm depth with minor ghosting at 71cm and 73cm, the 50kBq source situated at 74.7cm depth is reconstructed entirely at the closest depth of 75cm with no phasing in the 74cm plane and no ghosting, and the 10kBq source situated at 69.5cm is reconstructed entirely at 70cm with no phasing of this source having occurred at 69cm. The 5kBq source is just visible at its correct depth in the plane at 71cm but also with the same approximate reconstructed height at 70cm, 72cm, 73cm and even possibly 74cm. Such repeated occurrences indicates that no z-Cleaning of this source has taken place.

More detailed results for the three strongest sources are presented as profiles in Fig. 10 and in Tables 3 and 4, with SNR and depth calculations presented in Table 3.

### 6.1. *Pixellated Detector - Depth Profiles*

For the 100kBq source at plane separations of 2cm, 1cm and 0.5cm, all twenty trials for each give similar profiles to the mean profiles shown in the top three graphs in Fig. 10(a), with very little variation in each case, and the main peak being reconstructed at exactly the source depth of 72cm. At 2cm plane separation there is a single significant, but minor, ghost at 70cm, reflecting the example of the images in Fig. 9, and at 1cm plane separation, minor ghosting takes place in the voxels either side of the reconstructed main peak. The ghosting is relatively more marked for 1cm plane separation than for 2cm plane separation. For 0.5cm plane separation, the ghosts appear two voxels either side of the main peak, with high consistency. At 0.1cm plane separation all twenty trials reconstruct the main peak at the exact source depth of 72cm but not all trials follow the same profile. The bottom graph in Fig. 10(a) shows two profiles that represent the images having the most extreme positions of the ghosts which lie either side of and approximately 1cm from the main peak. The 0.1cm plane separation therefore represents



31

Figure 10: SNR depth profiles of the three sources using the pixellated detector.

Table 3: SNR, reconstructed depth ( $z$ ) and  $\text{PSLA}_z$  results obtained for twenty trials of the pixellated detector for the three strongest sources. For those values without errors quoted, the error is less than 0.001.

|                        | 100kBq at 72cm     | 50kBq at 74.7cm    | 10kBq at 69.5cm    |
|------------------------|--------------------|--------------------|--------------------|
| Critical plane SNR     | $247.9 \pm 1.2$    | $158.1 \pm 0.8$    | $42.6 \pm 0.4$     |
| 2cm plane separation   |                    |                    |                    |
| SNR                    | $187.9 \pm 0.6$    | $77.1 \pm 0.3$     | $12.7 \pm 0.1$     |
| $z$ (cm)               | $71.879 \pm 0.002$ | $74.394 \pm 0.003$ | $69.978 \pm 0.016$ |
| $\text{PSLA}_z$ (cm)   | 0.015              | 0.037              | $0.224 \pm 0.001$  |
| 1cm plane separation   |                    |                    |                    |
| SNR                    | $164.2 \pm 0.5$    | $85.3 \pm 0.3$     | $14.9 \pm 0.2$     |
| $z$ (cm)               | $71.931 \pm 0.001$ | $74.965 \pm 0.003$ | $69.663 \pm 0.101$ |
| $\text{PSLA}_z$ (cm)   | 0.009              | 0.017              | $0.095 \pm 0.001$  |
| 0.5cm plane separation |                    |                    |                    |
| SNR                    | $167.0 \pm 0.5$    | $88.5 \pm 0.3$     | $15.5 \pm 0.1$     |
| $z$ (cm)               | 71.993             | $74.990 \pm 0.001$ | $69.547 \pm 0.024$ |
| $\text{PSLA}_z$ (cm)   | 0.004              | 0.008              | 0.046              |
| 0.1cm plane separation |                    |                    |                    |
| SNR                    | $144.5 \pm 0.4$    | $74.7 \pm 0.6$     | $13.2 \pm 0.1$     |
| $z$ (cm)               | 71.900             | $74.997 \pm 0.002$ | $69.496 \pm 0.064$ |
| $\text{PSLA}_z$ (cm)   | 0.001              | 0.002              | 0.011              |

the only one studied so far for the 100kBq source using a pixellated detector where there is any variation in the positions of the ghosts.

For the 50kBq source at 74.7cm depth all twenty trials for plane separations of 2cm, 1cm and 0.5cm follow the same profiles as each of their respective graphs in Fig. 10(b) with little variation, while at 0.1cm plane separation only one of the trials (dashed line) deviates from the dark line profile shown in the bottom graph of Fig. 10(b). At 2cm plane separation there is clear phasing between 74 and 76cm with the higher peak being closest to the actual source depth and the values shared in roughly the correct proportions for this source. For the finer plane separations there is no phasing evident on any of the graphs but in all cases the main peak is reconstructed in the closest plane to the actual source depth, namely at 75cm.

For the 10kBq source at 69.5cm depth and at 2cm plane separation, all twenty trials reconstruct the source in the closest plane at 70cm depth with no evident phasing or ghosting in any other plane. The finer plane separations



Table 4: Pixellated detector: furthest distances of main reconstructed peaks from the actual source depth of twenty trials for each observation of the three strongest sources. All values are in cm. Asterisks denote actual source not lying at a plane to be decoded.

| Plane separation | Source         |                 |                 |
|------------------|----------------|-----------------|-----------------|
|                  | 100kBq at 72cm | 50kBq at 74.7cm | 10kBq at 69.5cm |
| 2                | 0              | 0.7*            | 0.5*            |
| 1                | 0              | 0.3*            | 0.5*            |
| 0.5              | 0              | 0.3*            | 0.5             |
| 0.1              | 0              | 0.3             | 0.5             |
| 0.02             | 0.12           |                 |                 |

give profiles that exhibit a single main peak with no phasing or ghosting evident. For 1cm plane separation all trials are similar to one of the two profiles shown, where the peak is reconstructed at either 69cm or 70cm, namely in one of the two planes closest to the actual source depth. For 0.5cm plane separation nineteen trials reconstruct the peak at the actual source depth of 69.5cm with the remaining trial being only one plane and 0.5cm away from the actual source depth. For 0.1cm plane separation peaks are reconstructed at various depths, three examples being given which include the two extremes at depths of 69cm and 69.8cm and a typical intervening example. Again the efficacy of the z-Clean technique is demonstrated for the three strongest sources.

For the 5kBq source all twenty trials for 0.5cm plane separation follow the same general profile shown in Fig. 8(b), with the profile itself being the mean for all the trials. The highest part of the graph reaches an SNR value of approximately 4 at around the actual source depth of 71cm, but there is no clear peak which indicates that no z-Cleaning has occurred and that significant artifacts in the form of repetitions of the reconstructed source are present in many of the nearby planes. Profiles for the other plane separations followed similar profiles to that in Fig. 8(b), indicating no z-Cleaning of this source, so these are not individually reported here.

## 6.2. Pixellated Detector - Reconstructed Source Depths

The depth location using the pixellated detector is very good for the three strongest sources for all plane separations, with all reconstructed depths being compatible with the actual source depths for all cases. As is the case for the continuous detector, the calculated depths of the reconstructed sources

that suffer a phasing error are generally slightly less accurately determined than those for which no phasing occurs. In particular the 50kBq source at 74.7cm is reconstructed between 0.265cm and 0.306cm from the actual depth although this result is still very good. Even in the worst case, namely the 10kBq source at 2cm plane separation, the reconstructed depth is only 0.478cm from the actual source depth. At plane separations of 1cm and finer the 10kBq source is able to be reconstructed to within 0.2cm of its actual depth, and the 100kBq source to within better than 0.1cm of its actual depth.

### 6.3. *Pixellated Detector - SNR and $PSLA_z$*

Table 3 shows that the SNR for the 100kBq reconstructed source is reduced by the implementation of z-Clean compared to critical plane observations for all plane separations, being generally more severe as the plane separation decreases, from 24% for 2cm plane separation to 42% for 0.1cm plane separation. Whereas the continuous detector experiences an unexpected SNR increase caused by the generation of incorrect candidates at different depths which remove detector counts that would otherwise have been assigned to potential ghosts adjacent to the main peak at 72cm depth, the use of a pixellated detector, which bins the counts in precisely defined pixels with no Gaussian spread, and hence no FWHM of detection, means that there would be no ghosting in the adjacent planes at 72cm and hence the detection of incorrect candidates at other depths and at the same lateral position has no effect on the overall variability, and hence no SNR increase occurs. Instead the use of z-Clean here comes at the expense of a reduction in the SNR compared to those of the critical plane observations.

For the 50kBq reconstructed source the SNR reduction is more severe, being between 44% for 0.5cm plane separation to 51% for 2cm plane separation. The SNR for 2cm plane separation is higher than that for 0.1cm plane separation. However the plane separations of 1cm and 0.5cm suffer less SNR degradation than 2cm plane separation, due probably to the source being located very close to the actual planes to be decoded and hence suffering a less severe phasing error. The SNR for the 10kBq reconstructed source, while remaining sufficiently high to render the source clearly visible, is quite severely impacted by the implementation of z-Clean, falling by 70% for 2cm plane separation and by the smaller amount of 64% for the best case for this source of 0.5cm plane separation, again probably due to the source lying at an actual plane to be studied for this particular plane separation. At

0.1cm plane separation the SNR decrease is more severe with a 69% decrease compared to the critical plane observations.

PSLA<sub>z</sub> for all sources improves with finer plane separations from 2cm to 0.1cm, ranging from 0.015cm to 0.001cm respectively for the 100kBq source, from 0.037cm to 0.002cm for the 50kBq source and from 0.224cm to 0.011cm for the 10kBq source.

#### 6.4. Pixellated Detector - 100kBq source only

As stated in Section 6, when using the pixellated detector all twenty trials for each plane separation successfully reconstructs the main source peak at the correct depth of 72cm, even down to 0.1cm plane separation (Fig. 10(a)). In view of this point, a further set of twenty trials was conducted of an observation of only a single 100kBq source at 72cm in the absence of the other three sources to ascertain whether z-Clean can reconstruct the main peak of this source at the same depth of 72cm but at the even finer depth resolution of 0.02cm. The reason that only this single source is observed is due to the infeasibly long run times that the z-Clean process requires for such fine resolution processing of fields containing multiple sources. Therefore we observe just this single source with the same background level of one count cm<sup>-2</sup> s<sup>-1</sup>. Fig. 11 shows portions of the profiles of three of the twenty trials, from depths of 71.4cm to 72.4cm. The main peaks of the example three trials are separated and small ghosts are visible for some of the trials at around 71.5cm and 71.6cm depth although for these and all the remaining twenty trials, similar sized ghosts to those in the figure were visible from around 70.5cm up to around 73.5cm beyond the range of the graph in the figure. For the twenty trials at this plane separation, the source depth is calculated at  $72.088 \pm 0.004$ cm, which is comparable to the results for the other plane separations as given in Table 3. Table 4 shows that the furthest plane that a reconstructed source appears for the twenty trials is only 0.12cm from the actual source depth.

## 7. Point Spread Function

The point spread function (PSF) of a coded aperture system can often be calculated theoretically. However, theoretical calculation of the PSF in the depth direction for images processed using the z-Clean technique, which we denote as PSF<sub>z</sub>, is extremely difficult. Therefore we attempt to determine a best estimate for PSF<sub>z</sub> by simulating an observation of an extremely strong

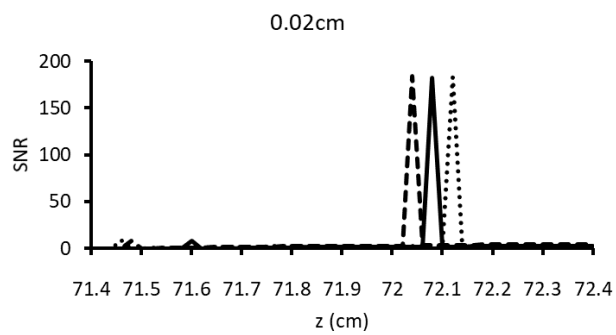


Figure 11: Portions of SNR depth profiles for a single 100kBq source using a pixellated detector.

single source in the absence of any background counts and performing z-Clean on the data. This has been done for both the continuous detector and pixellated detector, observing a 5MBq source in the centre of the FOV at 72cm depth (i.e. in the same position as the 100kBq source in the previous sections) and using the same system parameters as in Section 4 but with no background counts. This is done for each of the plane separations studied in Section 4. In each case, only one trial is conducted because the extremely long run times for the programs using such huge count numbers in conjunction with z-Clean renders multiple trials infeasible.

The depth profiles for the two detector types are shown in Fig. 12. For both detector types at all plane separations the main peak is reconstructed at the correct source depth of 72cm. In all cases ghosts are present either side of the main peak. The ghosting is roughly symmetrical when using the continuous detector for plane separations of 2cm and 1cm, and for the pixellated detector for 2cm plane separation. However for the remaining cases the ghosting is not symmetrically distributed and in some cases consists of three or more statistically significant ghosts. Furthermore it must be noted that the profiles are for a single source lying in a specific voxel and in the absence of the influence of other sources in the FOV. It is therefore to be expected that for other source positions in the FOV,  $\text{PSF}_z$  would take on a very large range of profiles with hugely varying numbers of and positions of ghosts.

## 8. Conclusions

This article presents an image processing technique, which we call z-Clean, that removes the repeated artifacts associated with image reconstruction in the 3D FOV when using a coded aperture imaging system. The technique includes determining the lateral positions and depths of point sources and removing artifacts caused on some planes by sources from another plane.

For a continuous detector with a 1cm FWHM detection capability at plane separations of 2cm, 1cm, 0.5cm and 0.1cm, the z-Clean technique is able to resolve three (100kBq, 50kBq and 10kBq) or four (also 5kBq) point sources very well, while at the same time significantly reducing to the level of minor ghosting the large artifacts caused by sources in other planes. The efficacy of z-Clean is thus demonstrated for the three stronger sources although there is some ghosting of the 100kBq and 50kBq sources, consisting of smaller peaks appearing in planes other than the one containing the source.

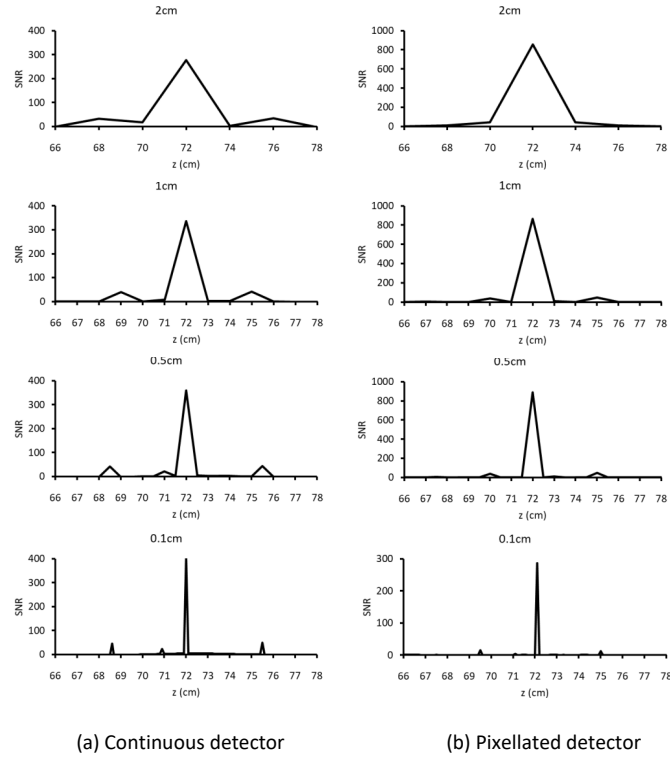


Figure 12: Estimated PSF<sub>z</sub> profiles for a single 5MBq source with no background.

832 The distributions of the ghosts show some small variability for the 100kBq  
 833 and 50kBq sources at 2cm plane separation and larger variability for finer  
 834 plane separations. The variability in the positions of the ghosts indicates  
 835 their presence as being non-systematic and containing a random component.  
 836 Ghosts typically appear up to around 2cm from the actual source depth.  
 837 Reconstructed images of the 10kBq source show a clear source peak for all  
 838 plane separations but with no ghosting evident, due to there being no can-  
 839 didates for this source in the z-Clean process other than the first one for  
 840 which a main peak is reconstructed. For the 5kBq source, z-Cleaning would  
 841 appear to occur only very rarely and even then to offer less accurate depth  
 842 location than for the stronger sources. The depth location and  $PSLA_z$  for all  
 843 plane separations are very good for the three strongest sources and individual  
 844 trials are able to reconstruct a source peak to 0.2cm or better from the ac-  
 845 tual source depth for the 100kBq source, with a worst performance of 0.7cm  
 846 from the actual source depth for the 50kBq source, which is still very good.  
 847 Sources that suffer a phasing error are generally less accurately located. The  
 848 excellent depth location and  $PSLA_z$  come at the expense of an impact on  
 849 the SNR, which for the strongest source increases unexpectedly due to the  
 850 incorrect detection of candidates lying at the same lateral position as the  
 851 actual source but at different depths, which suppresses ghosts that would  
 852 otherwise appear adjacent to the actual source in the correct plane. For the  
 853 weaker sources, SNR is reduced, in some cases quite severely, so the excellent  
 854 depth resolution made possible by z-Clean is traded off with an impact on  
 855 SNR.

856 For a pixellated detector with 0.2cm pixels, the efficacy of z-Clean is also  
 857 demonstrated, with the large repeated artifacts being removed and leaving  
 858 the three strongest sources clearly visible with only minor ghosting in some  
 859 other planes. The reconstruction of the source peaks and the ghosting is  
 860 quite consistent for the 100kBq and 50kBq sources at 2cm, 1cm and 0.5cm  
 861 plane separations, although there is some small variability in the ghosting  
 862 at 0.1cm plane separation. The reconstructed 10kBq source experienced no  
 863 ghosting but the reconstructed peaks appear at different depths for different  
 864 trials, although no further than 0.5cm from the actual source depth. As  
 865 was the case for the continuous detector, the depth location for the three  
 866 strongest sources is very good, being better than 0.5cm in all cases and  
 867 better than 0.1cm for the 100kBq source at plane separations of 1cm, 0.5cm  
 868 and 0.1cm.  $PSLA_z$  improves with SNR and finer plane separation, being as  
 869 good as 0.001cm for the 100kBq source at 0.1cm plane separation. Again the

870 very good depth location and  $\text{PSLA}_z$  come at the expense of a significant  
871 reduction in SNR, whose severity is higher for weaker sources.

872 As a technique and for certain situations, z-Clean is an efficacious method  
873 of removing the artifacts that typically appear in the planes of a 3D coded  
874 aperture imaging system when observing a source in a given plane and sug-  
875 gests that the results in earlier work by other authors, including Kazachkov  
876 et al. [8] and by Mu and Liu [13] might be improved upon. However this  
877 paper represents just a starting point in the idea of removing artifacts in  
878 3D coded aperture imaging, and further work in this area is possible which  
879 is beyond the scope of this article. Perhaps most importantly, such work  
880 could include observing different types of source distribution, in particular  
881 extended sources. This could be useful in medical imaging, for instance,  
882 where details of body organ structure are often required and hence good  
883 quality images of such extended objects are needed. Related to this could  
884 also be the study of the effect of different aperture throughput values, as well  
885 as what benefit, if any, different aperture throughput has when used to pro-  
886 cess images of extended sources using z-Clean [20]. Other future work could  
887 include investigating the use of z-Clean in the 3D image domain, rather than  
888 the 2D detector domain and a more detailed study into the use of detectors  
889 with different pixel size to bin size ratios, which would extend the work to  
890 include a wider range of detector parameters. Of particular interest to this  
891 entire field is the possibility of conducting experimental laboratory tests to  
892 observe real high energy sources using a physical position sensitive photon  
893 detector and applying z-Clean to the data.

## 894 9. Acknowledgments

895 The author would like to thank Drs. Mike Rutland and Ibrahim Has-  
896 san of Auckland Hospital, Dr. Berry Allen of the Waikato District Health  
897 Board and Drs. Paul Shutler and Stuart Springham of Nanyang Technolog-  
898 ical University, Singapore for very useful discussions during this work. Also  
899 the author would like to thank the two referees for their splendid feedback.

## 900 References

- 901 [1] L. Mertz and N.O. Young, “Fresnel transformations of images,” in *Pro-*  
902 *ceedings of the International Conference on Optical Instruments and*  
903 *Techniques*, K. J. Habell, ed. (Chapman and Hall, 1961), pp. 305–310.



- 904 [2] R.H. Dicke, "Scatter-hole cameras for X-rays and gamma rays," *Astro-*  
905 *phys. J. Lett.* **153**, L101–106 (1968).
- 906 [3] E.E. Fenimore and T.M. Cannon, "Coded aperture imaging with uni-  
907 *formly redundant arrays*," *Appl. Opt.* **17**, 337–347 (1978).
- 908 [4] E. Caroli, J.B. Stephen, G. Di Cocco, L. Natalucci and A. Spizzichino,  
909 "Coded aperture imaging in X- and gamma-ray astronomy," *Spa. Sci.*  
910 *Rev.* **45**, 349–403, (1987).
- 911 [5] G.K. Skinner, C.J. Eyles, A.P. Willmore, D. Bertram, M.J. Church,  
912 J.R.H. Herring, J. Ponman and M.P. Watt, "The Spacelab 2 X-ray tele-  
913 *scope - coded mask imaging in orbit*," *Astrophys. Lett. Comm.* **27**, 199–  
914 209 (1988).
- 915 [6] C. Winkler, T. J.-L. Courvoisier, G. Di Cocco, N. Gehrels, A. Giménez,  
916 S. Grebenev, W. Hermsen, J. M. Mas-Hesse, F. Lebrun, N. Lund, G.  
917 G. C. Palumbo, J. Paul, J.-P. Roques, H. Schnopper, V. Schönfelder,  
918 R. Sunyaev, B. Teegarden, P. Ubertini, G. Vedrenne and A. J. Dean,  
919 "The INTEGRAL mission," *Astron. Astrophys.* **411**, L1–6 (2003).
- 920 [7] W.L. Rogers, K.F. Koral, R. Mayans, P.F. Leonard, J.H. Thrall, T.J.  
921 Brady and J.W. Keyes, "Coded aperture imaging of the heart," *J. Nucl.*  
922 *Med.* **21**, 371–378 (1979).
- 923 [8] Y.P. Kazachkov, D.S. Semenov and N.P. Goryacheva, "Application of  
924 *coded apertures in medical gamma-ray cameras*," *Instr. Exper. Tech.*  
925 **50**, 267–274 (2007).
- 926 [9] A.A. Faust, R.E. Rothschild, P. Leblanc and J.E. McFee, "Development  
927 *of a coded aperture X-Ray backscatter imager for explosive device de-*  
928 *tection*," *IEEE Trans. Nucl. Sci.* **56**, 299–307 (2009).
- 929 [10] K.F. Koral, W.L. Rogers and G.F. Knoll, "Digital tomographic imaging  
930 *with a time-modulated pseudorandom coded aperture and anger cam-*  
931 *era*," *J. Nucl. Med.* **16**, 402–413 (1974).
- 932 [11] T.M. Cannon and E.E. Fenimore, "Tomographical imaging using uni-  
933 *formly redundant arrays*," *Appl. Opt.* **18**, 1052–1057 (1979).

- 934 [12] J.S. Fleming and B.A. Goddard, “An evaluation of techniques for sta-  
935 tionary coded aperture three-dimensional imaging in nuclear medicine,”  
936 Nucl. Instrum. Meth. Phys. Res. **221**, 242–246 (1984).
- 937 [13] Z. Mu and Y. Liu, “Aperture collimation correction and maximum-  
938 likelihood image reconstruction for near-field coded aperture imaging of  
939 single photon emission computerized tomography,” IEEE Trans. Med.  
940 Imaging **25**, 701–711 (2006).
- 941 [14] B.G. Clark, “An efficient implementation of the algorithm CLEAN,”  
942 Astron. Astrophys. **89**, 377–378 (1980).
- 943 [15] S.R. Gottesman and E.E Fenimore, “New family of binary arrays for  
944 coded aperture imaging,” Appl. Opt. **28**, 4344–4352 (1989).
- 945 [16] S.R. Gottesman and E.J. Schneid, “PNP - a new class of coded aperture  
946 arrays,” IEEE Trans. Nucl. Sci. **33**, 745–749 (1986).
- 947 [17] G. Ducros and R. Ducros, “Statistical analysis for coded-aperture  
948 gamma-ray telescope,” Nucl. Instrum. Meth. Phys. Res. **A221**, 49–53  
949 (1984).
- 950 [18] K. Byard and D. Ramsden, “Coded aperture imaging using imperfect de-  
951 tector systems,” Nucl. Instrum. Meth. Phys. Res. **A342**, 600–608 (1994).
- 952 [19] E.E. Fenimore, “Coded aperture imaging: predicted performance of uni-  
953 formly redundant arrays,” Appl. Opt. **17**, 3562–3570 (1978).
- 954 [20] J.J.M in’t Zand, J. Heise and R. Jager, “The optimum open fraction of  
955 coded apertures. With an application to the wide field X-ray cameras of  
956 SAX,” Astron. Astrophys. **288**, 665–6674 (1994).
- 957 [21] E.E. Fenimore and G.S. Weston, “Fast delta Hadamard transform,”  
958 Appl. Opt. **20**, 3058–3067 (1981).
- 959 [22] I.D. Jupp, K. Byard and A.J. Dean, “An improved sampling configura-  
960 tion for a coded aperture telescope,” Nucl. Instrum. Meth. Phys. Res.  
961 **A345**, 576–584 (1994).
- 962 [23] G.K. Skinner, “Sensitivity of coded mask telescopes,” Appl. Opt. **47**,  
963 2739–2749 (2008).

**Economics Working Paper Series**

*Faculty of Business, Economics and Law, AUT*

**Application of the CLEAN Algorithm to Three  
Dimensional Coded Aperture Imaging**

Kevin Byard

2020/14